Frontiers in Heat
and Mass Transfer

Tech Science Press

https://doi.org/10.32604/fhmt.2026.082595

ARTICLE

Thermomechanical Optimization Design of TGV Weight Respecting Restrictive Condition and Highly Sensitive Variables

Peng Guan*, **Ming-Ran Li and Si-Bo-Wen Wang**

Faculty of Aviation Engine, Shenyang Aerospace University, Shenyang, China

*Corresponding Author: Peng Guan. Email: 613511gp@163.com

Received: 18 March 2026; Accepted: 05 June 2026; Published: 31 August 2026

ABSTRACT: This paper develops a thermomechanical optimization method for turbo guide vane (TGV) weight reduction under restrictive conditions and highly sensitive variables. The proposed method integrates a flow-thermo-structural model, orthogonal experimental design (OED), and an optimization framework based on response surface methodology (RSM) and a genetic algorithm (GA). To address both the plastic limit and temperature distribution of the TGV, a new parameter termed the stress ratio is introduced as a constraint during optimization. Six highly sensitive variables were selected from ten cooling channel diameters using OED. Simulation results based on the thermal-fluid coupling model were validated against NASA reference data for the Mark-II TGV. The predicted and measured temperature distributions on the mid-span plane showed good agreement, with a maximum error of less than 7.5%. Compared with the original model, the optimized masses were reduced by 16.80% and 14.47% at stress ratios of 0.95 and 0.9, respectively. The stress ratio results from the RSM-based surrogate model were consistent with the simulations, demonstrating the accuracy of the thermomechanical optimization method. Furthermore, the location of the maximum stress ratio in the two optimized structures differed from that of the maximum stress, highlighting the necessity of introducing the stress ratio. The introduced stress ratio parameter and the proposed method for extracting highly sensitive factors provide a new approach for high-efficiency TGV optimization.

KEYWORDS: Turbo guide vane; orthogonal experimental design; response surface methodology; genetic algorithm; stress ratio; highly sensitive variables

1 Introduction

Improving the thrust-to-weight ratio is a primary objective in aero-engine design [1]. Two approaches exist to achieve this enhancement. The first involves increasing engine power by raising the turbine inlet temperature [2–4]. However, the progress has been slow due to limitations in high-temperature resistant materials. The second approach involves reducing the engine mass without compromising performance or structural strength [5]. Significant potential exists for weight reduction through the structural optimization of individual components. With advancements in simulation technology and computational performance, the finite element method (FEM) has become increasingly prevalent in structural optimization [6]. Although FEM is convenient, its computational workload is substantial for complex structures. Surrogate models establish the relationship between design variables and objectives using limited test data, thereby significantly reducing simulation complexity [7]. Several high-performance surrogate models have been proposed in recent decades [8], including the polynomial response surface method (RSM) [9], support vector regression [10–12], radial basis functions [13], extended radial basis functions [14], Kriging [15–17], moving

Copyright © 2026 The Authors. Published by Tech Science Press. This work is licensed under a Creative Commons Attribution 4.0 International License, which permits unrestricted use, distribution, and reproduction in any medium, provided the original work is properly cited.

least squares [18], artificial neural networks [19–21], and multivariate adaptive regression splines [22]. Among these, polynomial RSM is widely utilized due to its simple formulation and effective approximation capabilities [23,24].

The turbine guide vane (TGV) is a critical component of an aero-engine. Previous studies have focused on its weight reduction and performance improvement. For instance, Gallis et al. [25] optimized the blade profile of a high-pressure TGV using geometric parameterization, resulting in a reduced loss coefficient. Jiang et al. [26] optimized the shape parameters of spoon-shaped film cooling holes in TGVs using RSM. Huang et al. [27] further optimized dustpan-shaped holes on the suction surface using NSGA-II-RBFNN, obtaining a Pareto solution set that balanced cooling efficiency and flow coefficient. Zhang et al. [28] investigated the heat transfer characteristics of impingement cooling in a cavity by analyzing the influence of impingement hole and pin fin parameters. Wang et al. [29] conducted multi-configuration optimization on the internal cooling channels of TGVs, reducing the maximum temperature of C3X guide vanes by up to 50 K. Yu et al. [30] improved the heat transfer performance of internal cooling channels by optimizing hybrid rib structures and providing optimal design parameters. Wang et al. [31] employed the ANN-NSGA-II method to optimize the divergent cooling structure of C3X TGVs. Sun et al. [32] evaluated ceramic matrix composite (CMC) turbine vanes via geometric parameterization and a two-scale model. The advancement of artificial intelligence has provided new methods for the intelligent design of complex components such as TGVs. Evolutionary computing, particularly the genetic algorithm (GA), has demonstrated excellent performance in engineering optimization. Several studies have used GA to optimize the parameters of various TGV cooling structures [33,34]. First proposed by Andrew [35] in 1975, GA is a branch of evolutionary computation that transforms the optimization process into a procedure resembling biological evolution. GA is particularly suitable for complex optimization problems and is more efficient and accurate than conventional algorithms. It has been widely applied in combinatorial optimization, machine learning, signal processing, adaptive control, and artificial life.

In most previous studies, the objectives of TGV optimization were temperature and cooling efficiency. However, weight reduction is also a critical objective for improving aero-engine performance. Therefore, this paper develops an enhanced thermomechanical optimization design method to reduce TGV weight using a flow-thermo-structural model. The strength and mass of the TGV are optimized using orthogonal experimental design (OED), RSM, and GA. This study constructs an intelligent optimization framework suitable for TGV structures by combining GA with RSM. Additionally, a method for extracting highly sensitive design variables, an optimization method with constraints, and a stress ratio parameter that considers both temperature and stress are proposed. Ultimately, the methodology presented herein provides a valuable reference for the efficient weight reduction of turbine vanes.

2 Modeling and Simulation Methods

2.1 Flow-Thermo-Structural Model

The flow-thermo-structural model is a simulation framework encompassing both the cascade and the TGV. To determine the thermal strength of the TGV, the model is first fed into CFX software to simulate the conjugate heat transfer process. Subsequently, the temperature results for the TGV are imported directly into ANSYS software, where thermal stresses are solved using the thermal elastic FEM code. This study uses the Mark-II TGV as the research object, with the diameters of the internal cooling channels serving as the design variables.

The Mark-II TGV has a constant cross-section and can be modeled using curve segments derived from the polynomial fitting of characteristic points. NASA conducted a series of aerodynamic heat transfer tests on the Mark-II TGV. These tests measured static pressure, temperature, and convective heat transfer coefficient at the mid-span section of the TGV. The tests also documented the aerodynamic characteristics within the internal cooling channels [36]. Among these, the results from test condition No. 5411 are frequently used to evaluate the accuracy of computational fluid dynamics (CFD) results and the reliability of new turbulence models. This is because this condition involves both boundary layer transition phenomena and supersonic flow, which are challenging to simulate using CFD methods. The parameters for test condition No. 5411 are as follows: total inlet gas temperature of 788 K, total inlet gas pressure of 337,097 Pa, inlet gas relative turbulence of 6.5%, and static outlet gas pressure of 175,713 Pa. These data serve as the boundary conditions for the simulation.

The height, chord length, cascade width, and mounting angle of the Mark-II TGV are 76.2, 68.6, 130 mm, and 63.4°, respectively. Based on the geometric characteristics of the TGV, the gas domain is simplified as a horizontal cascade, as shown in Fig. 1. There are 10 cooling channels inside the TGV; their locations, numbers, and diameters are presented in Fig. 1 and Table 1. The TGV material is the superalloy GH3044; the material parameters used in this work are listed in Table 2 [37]. The gas is assumed to be an ideal gas. All boundaries are treated as no-slip walls, and periodic boundary conditions are applied to predict periodic flow. The selected turbulence model is the four-equation shear stress transport (SST) γ–θ model, which calculates turbulent kinetic energy, turbulence frequency, transition sources, and transition momentum thickness. This model is suitable for simulating boundary layer transition and conjugate heat transfer. The influence of gas kinetic energy on heat transfer is accounted for using the total energy model.

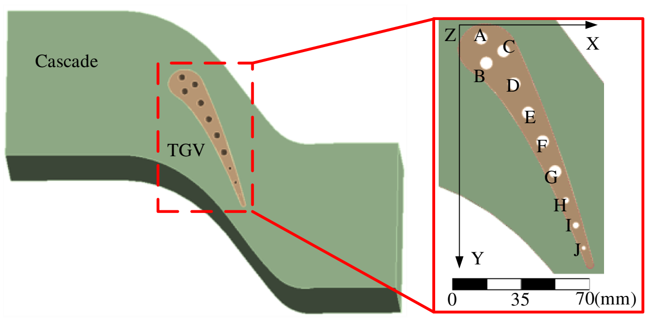

Figure 1: Geometric model of the cascade and TGV.

Table 1: Simulation conditions for cooling holes with different diameters.

Serial Number	Diameter (mm)	Flow (g/s)	Total Inlet Temperature (K)	Convection Heat Transfer Coefficient (W/(m^2·K))
A	6.30	24.33	326.26	1922.97
B	6.30	23.42	316.68	1854.98
C	6.30	23.55	322.18	1869.78
D	6.30	24.98	328.95	1966.59
E	6.30	23.46	308.52	1850.01
F	6.30	22.34	305.46	1775.54
G	6.30	23.55	313.15	1863.24

(Continued)

Table 1 (continued)

Serial Number	Diameter (mm)	Flow (g/s)	Total Inlet Temperature (K)	Convection Heat Transfer Coefficient (W/(m^2·K))
H	3.10	7.772	335.28	2799.84
I	3.10	5.138	330.46	2011.70
J	1.98	3.329	354.71	3266.68

Table 2: Material parameters of GH3044 [37].

Parameters	Scope
Temperature, K	293–1273
Thermal expansion coefficient, $\times 10^{-5}$ K^{-1}	1.03–1.35
Young modulus, GPa	207–123
Poisson ratio	0.28–0.36
Shear modulus, $\times 10^{11}$ Pa	0.81–0.45
Heat transfer coefficient, W/m·K	13.9–25.9
Density, kg/m^3	8680
Specific heat, J/kg·K	493–594
Yield strength, MPa	775–185

Fig. 2 presents the schematic diagram of the TGV support employed in the thermoelastic simulation. To replicate the actual mounting configuration and prevent rigid body displacement, an extended section is added to the end of the cooling channels, as illustrated in Fig. 2. A fixed support is applied to the bottom surface of this elongated section. The Bilinear Kinematic hardening model is utilized to simulate elastic-plastic behavior. This plasticity model assumes that the total stress range equals twice the yield stress, thereby accounting for the Bauschinger effect. It is applicable to materials adhering to the von Mises yield criterion, which includes most metals.

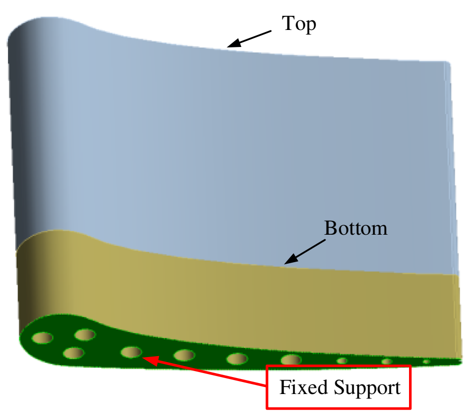

Figure 2: Schematic diagram of the TGV support.

The TGV and cascade are meshed using the sweep grid method. To establish a reliable baseline, the mesh topology and refinement strategy in this study are adopted from established, comprehensively validated studies on the Mark-II TGV model [38,39]. Specifically, the grids near the TGV wall are refined relative to the rest of the cascade to capture boundary layer flow details. The first layer thickness near the wall is 1 μm, with an expansion ratio of 1.2. The resulting finite element model is shown in Fig. 3.

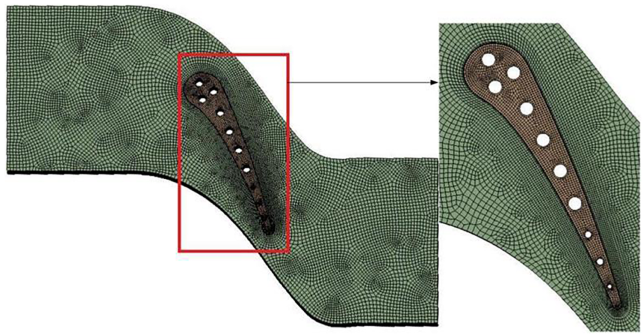

Figure 3: Meshes of the cascade and TGV.

To verify grid independence and ensure the reliability of the adopted mesh topology for the present model, a mesh independence study is conducted. Multiple grid densities are evaluated, as shown in Fig. 4. When the total number of nodes increases from 668,792 to 795,226, the relative error in the temperature distribution is less than 1%. This indicates that further increasing the grid density has a negligible effect on the computational results. Therefore, the mesh configuration with 668,792 nodes and approximately 630,000 cells is adopted for the model optimization in this study.

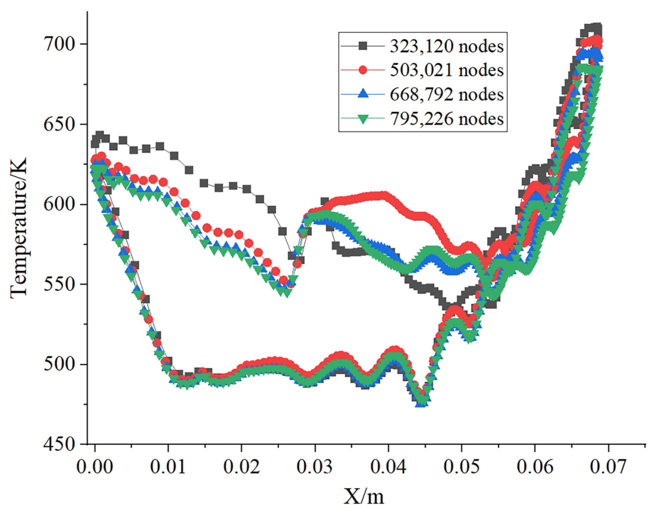

Figure 4: Surface temperature variations along the X-axis for various mesh resolutions.

Furthermore, since the cooling channel diameters vary continuously during optimization, an automated adaptive meshing strategy driven by geometric feature recognition is implemented in ANSYS Workbench. To ensure that the validated refinement approach remains applicable across a wide range of hole diameters, advanced size functions based on proximity and curvature are activated. As the hole sizes change dynamically in each optimization iteration, the meshing algorithm automatically detects varying geometric curvatures and continuously adjusts the local element size and node distribution around the cooling holes. This robust, geometry-adaptive strategy ensures that the local mesh density near the cooling holes, which governs critical stress ratio calculations, is automatically refined and remains consistently reliable without manual intervention.

2.2 Heat Transfer Boundary Conditions of Inner Cooling Holes

The optimization variables in this study are the diameters of the cooling holes. Because the size of the cooling air domain depends on these diameters, an experimental correlation model for calculating the convective heat transfer coefficient is developed based on the heat transfer theory of circular tubes to avoid the complexities of adaptive mesh generation and enhance computational efficiency. The heat transfer mechanism in the cooling holes is forced convective heat transfer in tubes without phase change. The convective heat transfer coefficients for each cooling hole can be estimated using Eq. (1):

$$h = \frac{\lambda Nu}{d} \tag{1}$$

where h is the convective heat transfer coefficient of the gas, λ is the thermal conductivity of the gas, d is the diameter of the cooling hole, and Nu is the Nusselt number. The formula for calculating the Nusselt number is as follows [40]:

$$Nu = 0.023\mathrm{Re}^{0.8}\mathrm{Pr}^{0.4} \tag{2}$$

where Re and Pr are the Reynolds number and Prandtl number, respectively. Re and Pr can be calculated by

$$\mathrm{Re} = \frac{u\rho d}{\mu} \tag{3}$$

$$\mathrm{Pr} = \frac{v}{a} \tag{4}$$

where u is the gas flow rate, ρ is the gas density, μ is the dynamic viscosity of the gas, v is the kinematic viscosity of the gas, and a is the thermal diffusivity of the gas. u and a are expressed as

$$u = \frac{4m}{\pi\rho d^2} \tag{5}$$

$$a = \frac{\lambda}{\rho C_p} \tag{6}$$

where m is the mass flow rate of the gas in the cooling hole, and C_P is the specific heat capacity of the gas. Combining the above equations yields the experimental correlation model as follows:

$$h = 0.023 \times 4^{0.8} \times \frac{m^{0.8} \cdot C_p^{0.4} \cdot \lambda^{0.6}}{d^{1.8} \cdot \mu^{0.4} \cdot \pi^{0.8}} \tag{7}$$

The convective heat transfer coefficient for each cooling hole in the Mark-II TGV is obtained using Eq. (7), as shown in Table 1.

2.3 OED Theory

There are ten cooling channels inside the TGV body. To improve the original design scheme, it is necessary to identify which design variables significantly influence TGV performance. OED is employed to analyze the importance of these design variables. OED is a method that uses orthogonal arrays to arrange and analyze multi-variable tests [41]. It evaluates a representative subset of all test combinations and infers the results for the entire combination space, thereby addressing the high computational workload associated with comprehensive analysis of the full test set. Range analysis and variance analysis are two methods commonly used to analyze OED data. Range analysis intuitively ranks the influence of each factor on the result, reflecting the sensitivity of the design variables. Both range and variance analyses help estimate experimental error and improve accuracy. The expression for the range is as follows:

$$N_i = \max M_{ij} - \min M_{ij} \tag{8}$$

where N_i is the range of the i-th variable, and M_{ij} is the mean of all results at the j-th level of the i-th variable.

2.4 RSM Method

RSM constructs mathematical expressions relating output results to design variables [42]. These expressions establish a purely numerical correspondence without inherent physical meaning. A widely used RSM model is the second-order response surface polynomial function [43], which is formulated as follows:

$$Y = \beta_0 + \sum_{i=1}^{k} \beta_i x_i + \sum_{i=1}^{k} \beta_{ii} {x_i}^2 + \sum_{i<j}\sum \beta_{ij} x_i x_j + \varepsilon \tag{9}$$

where Y is the predicted response, x_i and x_j are the values of the design variables, k is the number of design variables, β_0 is the constant term, β_i ($i = 1, \ldots, k$) are the linear coefficients, β_{ii} ($i = 1, \ldots, k$) are the quadratic coefficients, and β_{ij} (i, $j = 1, \ldots, k$) are the interaction coefficients. Various RSM designs exist, including full factorial design, central composite design (CCD), Box-Behnken design, D-optimal design, orthogonal design, and homogeneous design. The CCD method is selected in this study because it efficiently estimates first- and second-order terms.

3 Results and Discussion

3.1 Analysis of Standard Mark-II TGV Simulation Results

To verify the accuracy of the flow-thermo-structural model, the experimental results of the standard Mark-II TGV are compared with the simulation results, as shown in Fig. 5. Both the simulated temperature and pressure results align well with the experimental data. The maximum error occurs on the suction side of the TGV, attributed to transitional flow and shock phenomena. Although simulating transitional flow and shock is challenging, the SST γ–θ turbulence model yields results acceptable for engineering applications. The maximum relative error between the simulation and the test is 7.15%, validating the accuracy of the employed simulation method.

Traditionally, if irreversible thermal deformation occurs during operation, the TGV design is considered a failure. Thus, the structural design of a TGV is determined by its plastic performance under the most severe working conditions. However, because the yield stress governing this plastic performance varies with temperature, assessing the feasibility of a design scheme solely based on isothermal yield stress is difficult. To address this issue, a strength judgment parameter named the stress ratio R is defined, considering both temperature and stress, as expressed below:

$$R = \frac{\sigma(T)}{\sigma_{\mathrm{P}}(T)} \tag{10}$$

where $\sigma(T)$ is the thermal stress of the Mark-II TGV, and $\sigma_p(T)$ is the yield stress function of GH3044 [37]. $\sigma_p(T)$ is a single-valued function of temperature T, calculated using the following equation:

$$\sigma_P(T) = 419.3 - 0.4347 \cdot T + 6.298 \times 10^{-4} \cdot T^2 - 3.662 \times 10^{-7} \cdot T^3 \tag{11}$$

$\sigma(T)$ represents the von Mises stress σ_e of the TGV, which is expressed as

$$\sigma_e = \frac{1}{\sqrt{2}}\sqrt{\left(\sigma_x - \sigma_y\right)^2 + \left(\sigma_y - \sigma_z\right)^2 + \left(\sigma_z - \sigma_x\right)^2 + 6\left(\tau_{xy}^2 + \tau_{yz}^2 + \tau_{zx}^2\right)} \tag{12}$$

where σ_x, σ_y, and σ_z are the normal stress components in the x, y, and z directions, respectively. τ_{xy}, τ_{yz}, and τ_{zx} are the shear stress components on the xy, yz, and zx planes, respectively.

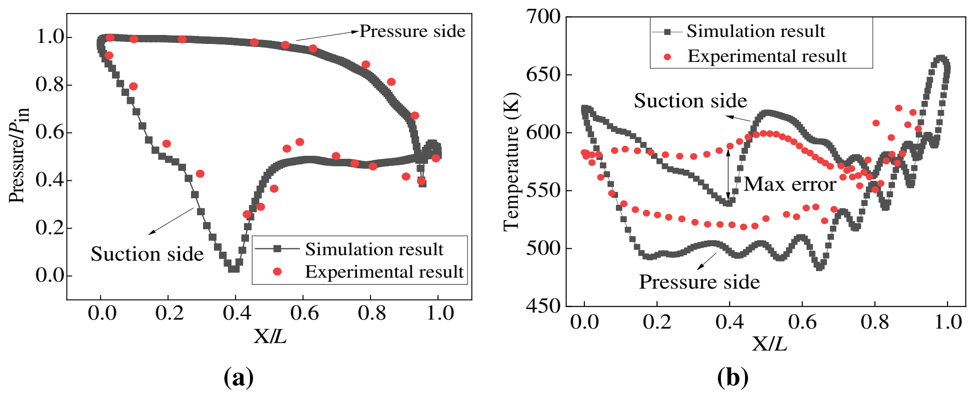

Figure 5: Comparison of experimental and simulation results at mid-span. (**a**) Pressure distribution. Pressure is normalized by the total inlet gas pressure (P_{in} = 337,097 Pa), and the streamwise coordinate is normalized by the blade axial length (L = 70 mm). (**b**) Temperature distribution. Temperature is shown in Kelvin, using the same normalized coordinate X/L.

Fig. 6 displays the contours of the simulation results. As shown in Fig. 6a, the temperature on the trailing edge surface is higher than that in other regions, reaching a maximum of 682.9 K. The temperature around cooling channel B is the lowest, reaching a minimum of 411.2 K. As shown in Fig. 6b, the stress at the bottom of the TGV is greater than that at the top, and the stress at the leading edge is higher than that in the remaining parts. The maximum stress of 345.2 MPa occurs in channel G, while the minimum stress of 1.3 MPa is located at the top surface of the trailing edge. Fig. 6c shows the simulation results for the stress ratio. The stress ratio distribution approximates the stress distribution. The maximum stress ratio is 1.15 at the bottom of channel G, while the minimum is close to 0 at the top of the trailing edge. Since the maximum stress ratio of the original model exceeds 1, the original design scheme is deemed unreasonable.

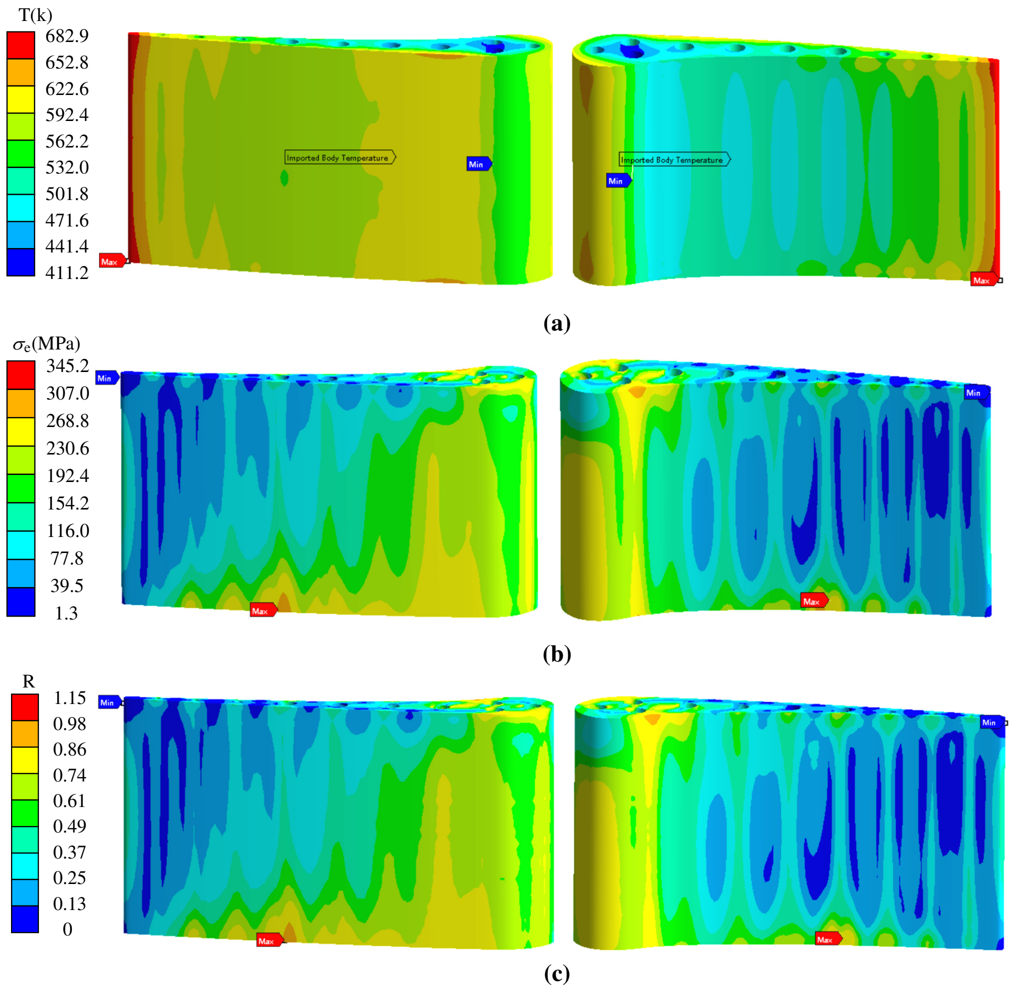

Figure 6: Simulation results of the standard Mark-II TGV. (**a**) Temperature. (**b**) Equivalent stress. (**c**) Equivalent stress ratio.

3.2 Selection Method for Highly Sensitive Variables

The diameters of the 10 cooling channels are analyzed using the OED method to identify highly sensitive variables. An OED table comprising 10 variables and 5 levels is employed. The letters A–J in Table 3 correspond to the diameters of the 10 cooling holes labeled in Fig. 1. The diameters for each variable at each level are presented in Table 3.

Table 3: Diameters of the 10 cooling channels (A–J) at five OED levels.

	A (mm)	B (mm)	C (mm)	D (mm)	E (mm)	F (mm)	G (mm)	H (mm)	I (mm)	J (mm)
Level 1	3.00	3	3	3	3	3	3	1	1	1
Level 2	4.75	4.75	4.75	6.25	5.5	4.75	4	2	1.75	1.5
Level 3	6.5	6.5	6.5	9.5	8	6.5	5	3	2.5	2
Level 4	8.25	8.25	8.25	12.75	10.5	8.25	6	4	3.25	2.5
Level 5	10	10	10	16	13	10	7	5	4	3

Figs. 7 and 8 present the graphical analysis of TGV mass obtained via OED and the corresponding range analysis, respectively. As illustrated in Fig. 7, TGV mass decreases as the diameter increases. Fig. 8 indicates that channel D exhibits the highest sensitivity to TGV mass, followed by channel E. Channels A, B, C and F demonstrate identical, relatively low sensitivity. The sensitivity of channels G, H, I and J is lower than that of the other six channels. Overall, channel sensitivity to TGV mass is positively correlated with diameter.

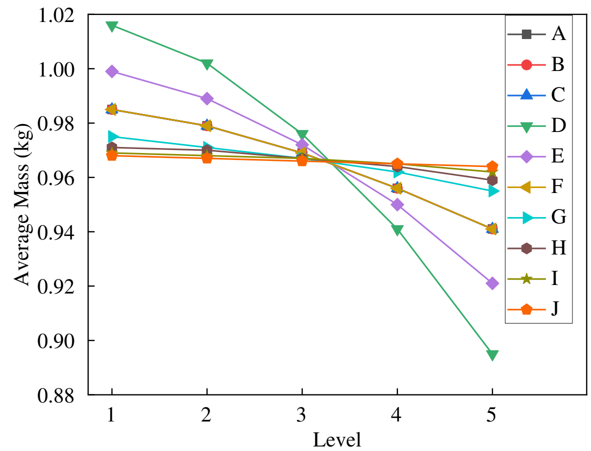

Figure 7: Visual analysis chart of average mass.

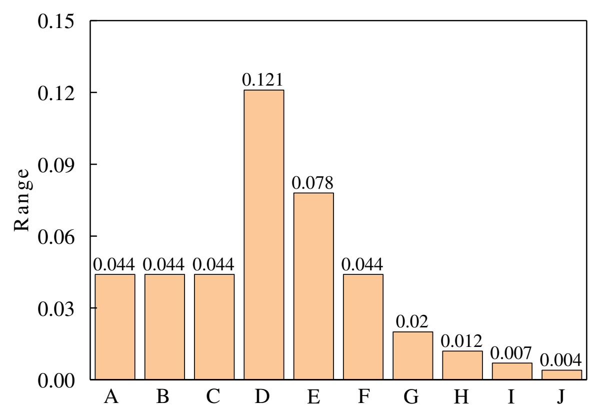

Figure 8: Range analysis of TGV mass.

Based on the TGV mass analysis, variables are classified into high- and low-sensitivity groups. Channels A, B, C, D, E and F are high-sensitivity variables, while the remaining channels are low-sensitivity variables. Fig. 9a presents a visual analysis of the stress ratio for the high-sensitivity variables. As shown in Fig. 9a, as channel A increases, the TGV stress ratio initially increases, stabilizes, and then decreases. With an increase in channel B, the stress ratio first decreases, then rises, and finally decreases slightly. For channel C, the stress ratio decreases monotonically. For channels D and F, the stress ratio rises slightly before increasing rapidly. For channel E, the stress ratio rises, falls and then increases rapidly. Fig. 9b shows the visual analysis of the stress ratio for the low-sensitivity variables. As shown in Fig. 9b, as channel G increases, the TGV stress ratio increases, decreases, and then increases again. For channels H, I and J, the stress ratio first decreases, then increases, and finally decreases.

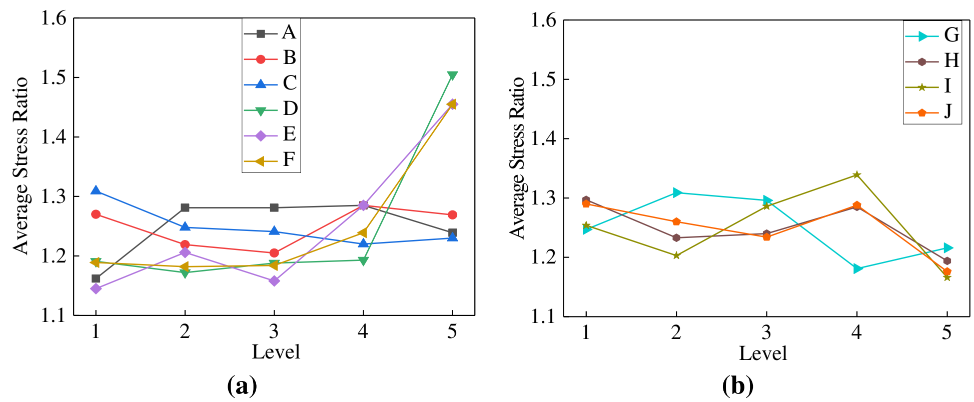

Figure 9: Visual analysis of the TGV stress ratio. (**a**) Stress ratio of high-sensitivity parameters. (**b**) Stress ratio of low-sensitivity parameters.

Fig. 10 shows the range analysis graph of the TGV stress ratio. Channels D, E, and F are the three most sensitive variables affecting the TGV stress ratio, followed by channels A, G and I, while the remaining channels exhibit lower sensitivity. There is no correlation between the cooling channel diameter and stress ratio sensitivity. Combining Figs. 7 and 9b, the mass and stress ratio of channels H, I and J reach their minimum values simultaneously when their diameters are maximized. Therefore, the optimal diameters for these three channels are their maximum values. For channel G, the stress ratio is minimized at level 4, with little sensitivity to TGV mass; thus, the optimal value for channel G is level 4. The optimal values for the remaining six channels cannot be determined by this method and require further optimization using RSM.

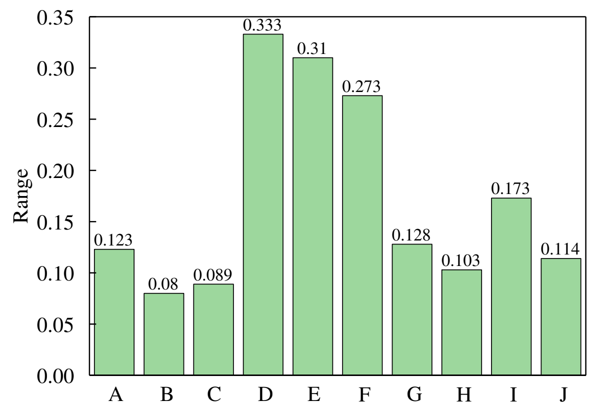

Figure 10: Range analysis chart of the TGV stress ratio.

3.3 Establishment of the Optimization Method under Restrictive Conditions

For highly sensitive variables, this study employs CCD within the RSM framework. The variable ranges for the RSM are consistent with those listed in Table 1. A CCD method involving six variables requires 86 experimental sets, whereas ten variables would necessitate more than 500 sets. This demonstrates that the preliminary OED analysis significantly reduces the computational workload of RSM.

The TGV mass can be calculated directly from the diameters of the individual cooling channels without relying on RSM. In this study, a second-order inverse proportional function response model is used to fit the relationship between the maximum stress ratio of the TGV and the cooling channel diameters, as shown in Eq. (13):

$$
\begin{aligned}
y^{-1} = {} & 1.052 + 0.01163A - 0.02762B - 0.01077C - 0.05984D - 0.03983E - 0.01952F \\
& + 0.0004065A \cdot B + 0.005933A \cdot C + 0.001991A \cdot D - 0.003673A \cdot E - 0.001971A \cdot F \\
& - 0.02799B \cdot C + 0.03384B \cdot D + 0.006510B \cdot E + 0.004259B \cdot F + 0.04831C \cdot D \\
& + 0.01272C \cdot E + 0.008049C \cdot F + 0.02060D \cdot E + 0.02153D \cdot F + 0.02765E \cdot F \\
& + 0.05918A^2 + 0.04208B^2 - 0.008597C^2 - 0.1765D^2 - 0.1078E^2 - 0.09455F^2
\end{aligned} \tag{13}
$$

where y represents the maximum stress ratio of the TGV, and A, B, C, D, E and F denote the diameters of the corresponding channels, respectively. The coefficient of determination for Eq. (13) is 0.9523, which is close to 1, indicating that the model fits the training data well.

To globally assess the predictive performance of the response surface model, leave-one-out cross-validation (LOOCV) is employed. Given a dataset of N design points, each point i ($i = 1, \ldots, N$) is sequentially removed, and a response surface model is fitted to the remaining N–1 points. This model is then used to predict the response at the removed point, yielding a predicted residual. The process is repeated for all N points, and the predicted residual sum of squares (PRESS) is calculated as

$$PRESS = \sum_{i=1}^{N} \left(y_i - \hat{y}_{i(i)} \right)^2 \tag{14}$$

where y_i is the actual FEM-computed response and $\hat{y}_{i(i)}$ is the predicted response from the model fitted without point i. The predicted R^2 is then computed as

$$R^2_{pred} = 1 - \frac{PRESS}{SS_{total}} \tag{15}$$

where $SS_{total} = \sum_{i=1}^{N} (y_i - \overline{y})^2$ is the total sum of squares. Additionally, the adequate precision (signal-to-noise ratio) is calculated as

$$AdeqPrecision = \frac{\max\left(\hat{y}\right) - \min\left(\hat{y}\right)}{\sqrt{MSE \cdot \frac{p}{n}}} \tag{16}$$

All statistical validations are performed using Design-Expert software (version 13, Stat-Ease Inc.). Based on the LOOCV procedure, the PRESS statistic is calculated to be 0.015. Consequently, the model exhibits a predicted R^2 of 0.9375, which is in excellent agreement with the adjusted R^2 of 0.9479, indicating strong global predictive ability. The adequate precision is 10.6891 (>4), confirming a sufficient signal-to-noise ratio for engineering predictions. This LOOCV-based validation provides a robust global assessment of the surrogate model's predictive capability [44].

The objective of the optimal design is to minimize the TGV mass while maintaining a TGV stress ratio of less than 1, a process referred to as constrained optimization. While RSM can optimize a single objective by differentiating the relevant equations, solving optimization problems with restrictive constraints is challenging. Therefore, this study establishes an optimization method for the Mark-II TGV under constrained conditions by combining GA with RSM.

Fig. 11 illustrates the process of the constrained optimization method for the Mark-II TGV. The procedure is detailed as follows. First, the range of each variable is input, followed by coding, generation of the initial population, and operations such as crossover and mutation. Next, the individual genes are decoded to obtain specific variable values, and the corresponding TGV mass and maximum stress ratio are calculated.

The algorithm then determines whether the TGV maximum stress ratio is less than 1. If the condition is met, the process proceeds to the next step; otherwise, the TGV mass is penalized by setting it to three times the calculated value. Finally, the population is filtered based on the TGV mass, and the output condition is evaluated. If the condition is not satisfied, the GA crossover and mutation operations are repeated; if satisfied, the optimal variable values are output.

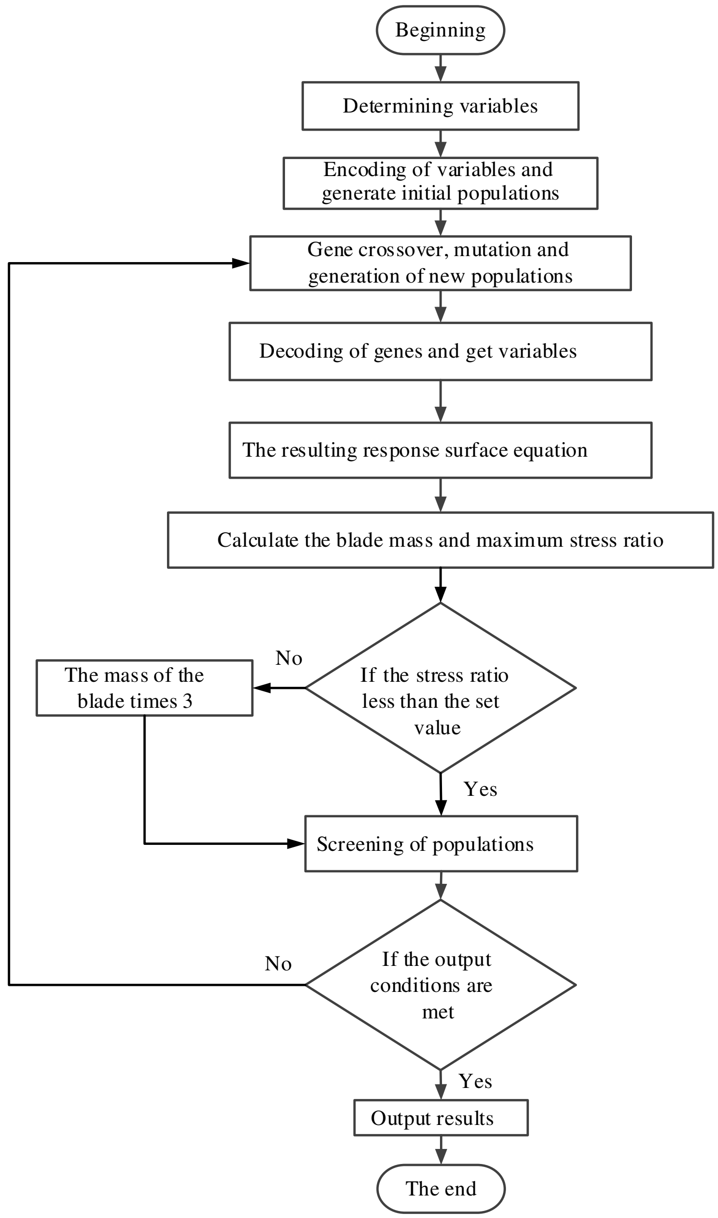

Figure 11: Optimization process under restrictive conditions.

3.4 Analysis of Optimization Results

To accommodate fluctuations in TGV operating conditions, a strength margin is incorporated into the optimization process by maintaining the maximum stress ratio below 1. In this study, stress ratios of 0.95 and 0.9 are evaluated. The resulting cooling channel variables for the TGV at these stress ratios are presented in Table 4. The mass of the Mark-II TGV under standard cooling channel conditions is 1.03 kg. At a maximum stress ratio of 0.95, the mass is 0.857 kg, representing a 16.80% reduction compared to the standard TGV. At a maximum stress ratio of 0.9, the mass is 0.881 kg, corresponding to a 14.47% reduction relative to the standard model.

Table 4: Optimization results of variables for the Mark-II TGV.

	A (mm)	B (mm)	C (mm)	D (mm)	E (mm)	F (mm)	G (mm)	H (mm)	I (mm)	J (mm)
$R = 0.95$	10	10	10	12.448	9.515	7.404	6.3	3.1	3.1	1.98
$R = 0.9$	10	3	10	12.353	10.19	7.684	6.3	3.1	3.1	1.98

Fig. 12 compares the structure before and after optimization. As illustrated, the diameters of most optimized channels increase compared to those of the standard TGV, except for channel B. Channels D, E and F in the 0.95 stress ratio case are slightly larger than those in the 0.9 case, while all other channels retain the same diameter. The enlargement of most channels facilitates TGV weight reduction. Conversely, channel B exhibits stress concentration; reducing its diameter increases local stiffness and mitigates stress. Although this reduction slightly decreases cooling capacity, the effect is minimal because the original temperature at this location is lower than that in other regions. This explains the reduced diameter of channel B in the optimized design.

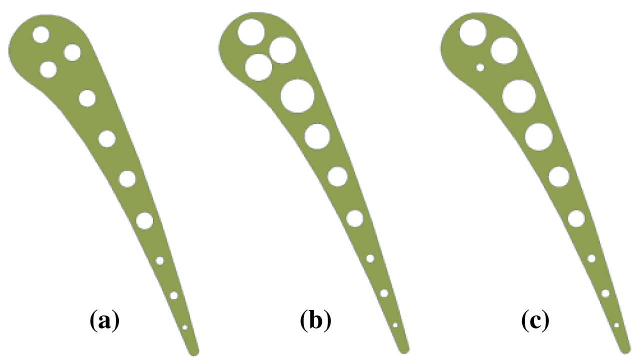

Figure 12: Structural comparison of the Mark-II TGV before and after optimization. (**a**) Original model. (**b**) $R = 0.95$. (**c**) $R = 0.9$.

To verify the accuracy of the GA-based Mark-II TGV optimization method and evaluate the optimized structure, simulations are conducted on the optimized TGV. Fig. 13 presents the simulation results for a TGV with a maximum stress ratio of 0.95. As shown in Fig. 13a, the trailing edge temperature is elevated, with a maximum of 688.9 K at the bottom of the trailing edge. Conversely, the temperature in cooling channel B is lower, reaching a minimum of 380.7 K at the channel midpoint. Compared to the standard TGV, the maximum temperature is increased by 6.0 K, while the minimum temperature is decreased by 30.5 K. Fig. 13b illustrates the stress distribution. Stress at the bottom of channel C is higher than that in other regions. The maximum stress is 309.1 MPa, while the minimum stress of 1.3 MPa occurs at the top of the trailing edge. The maximum stress is reduced by 36.1 MPa compared to the standard TGV, whereas the minimum stress remains unchanged. Fig. 13c displays the stress ratio distribution, which closely mirrors the stress distribution. The maximum stress ratio is 0.94 at the bottom of channel C, while the minimum is near zero at the top of the trailing edge. The achieved maximum stress ratio of 0.94 approximates the target value of 0.95, validating the optimization method's accuracy. Although the location of the maximum stress ratio resembles that of the maximum stress, they do not coincide, underscoring the necessity of stress ratio analysis.

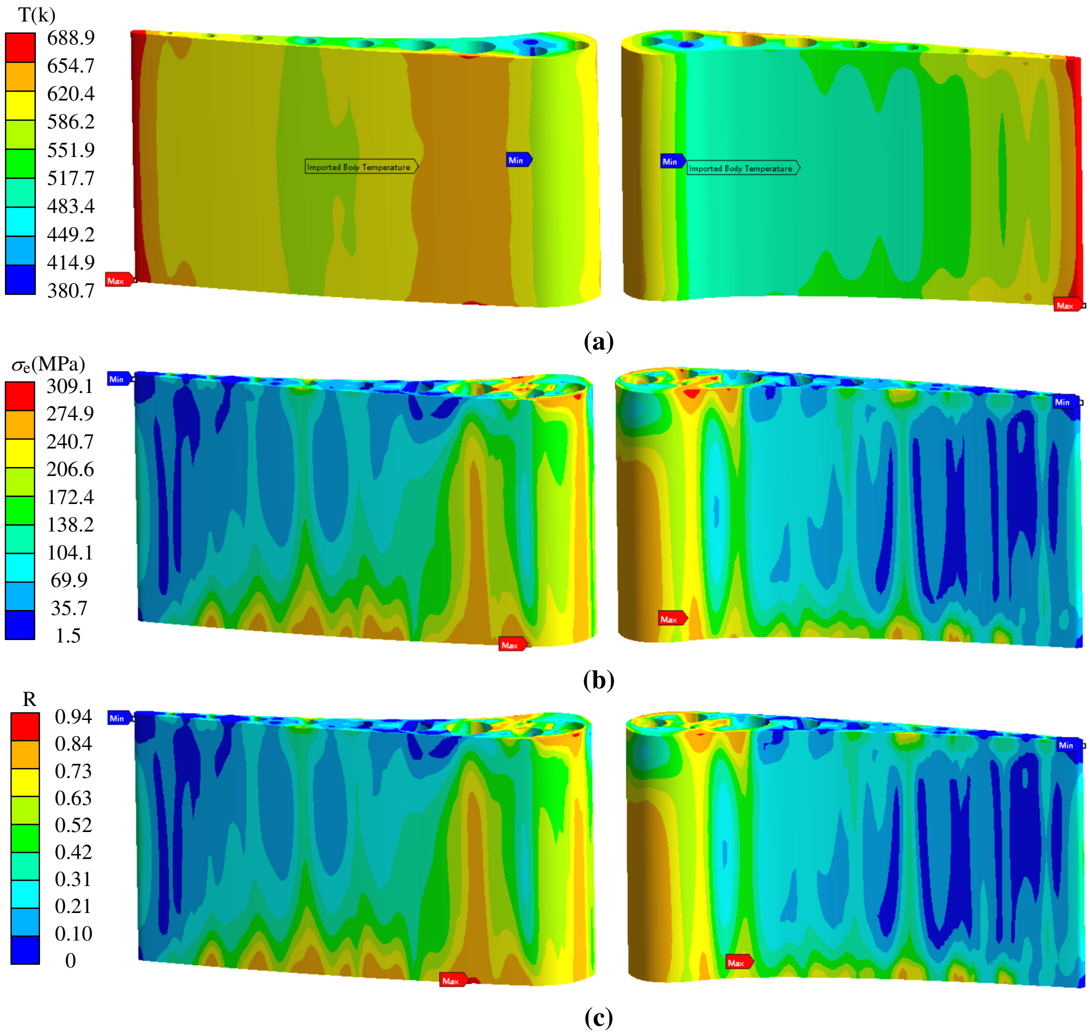

Figure 13: Simulation results of the Mark-II TGV when the maximum stress ratio is 0.95. (**a**) Temperature. (**b**) Equivalent stress. (**c**) Stress ratio.

Fig. 14 presents the simulation results for the TGV with a maximum stress ratio of 0.9. Fig. 14a illustrates the temperature distribution. The trailing edge exhibits higher temperatures, with a maximum of 688.6 K located at the top of the trailing edge. Conversely, the temperature in cooling channel B is lower, with a minimum of 380.4 K situated in the middle section of channel B. Compared to the standard TGV, the maximum temperature is increased by 5.7 K, while the minimum temperature is decreased by 30.8 K. Fig. 14b displays the thermal stress simulation results. Stress is higher at the bottom of the leading edge and lower in other regions. The maximum stress of 308.6 MPa occurs at the bottom of channel C, while the minimum stress of 1.3 MPa is found at the top of the trailing edge. The maximum stress is reduced by 36.6 MPa compared to the standard model, whereas the minimum stress remains unchanged. Fig. 14c shows the distribution of the stress ratio, which approximates that of the thermal stress. The maximum stress ratio is 0.9 at the bottom of channel H, and the minimum is close to 0 at the top of the trailing edge. The maximum stress ratio aligns with the set value, further validating the accuracy of the optimization method. Although the location of the maximum stress ratio is similar to that of the maximum stress, they do not coincide. This discrepancy underscores the necessity of introducing stress ratio analysis.

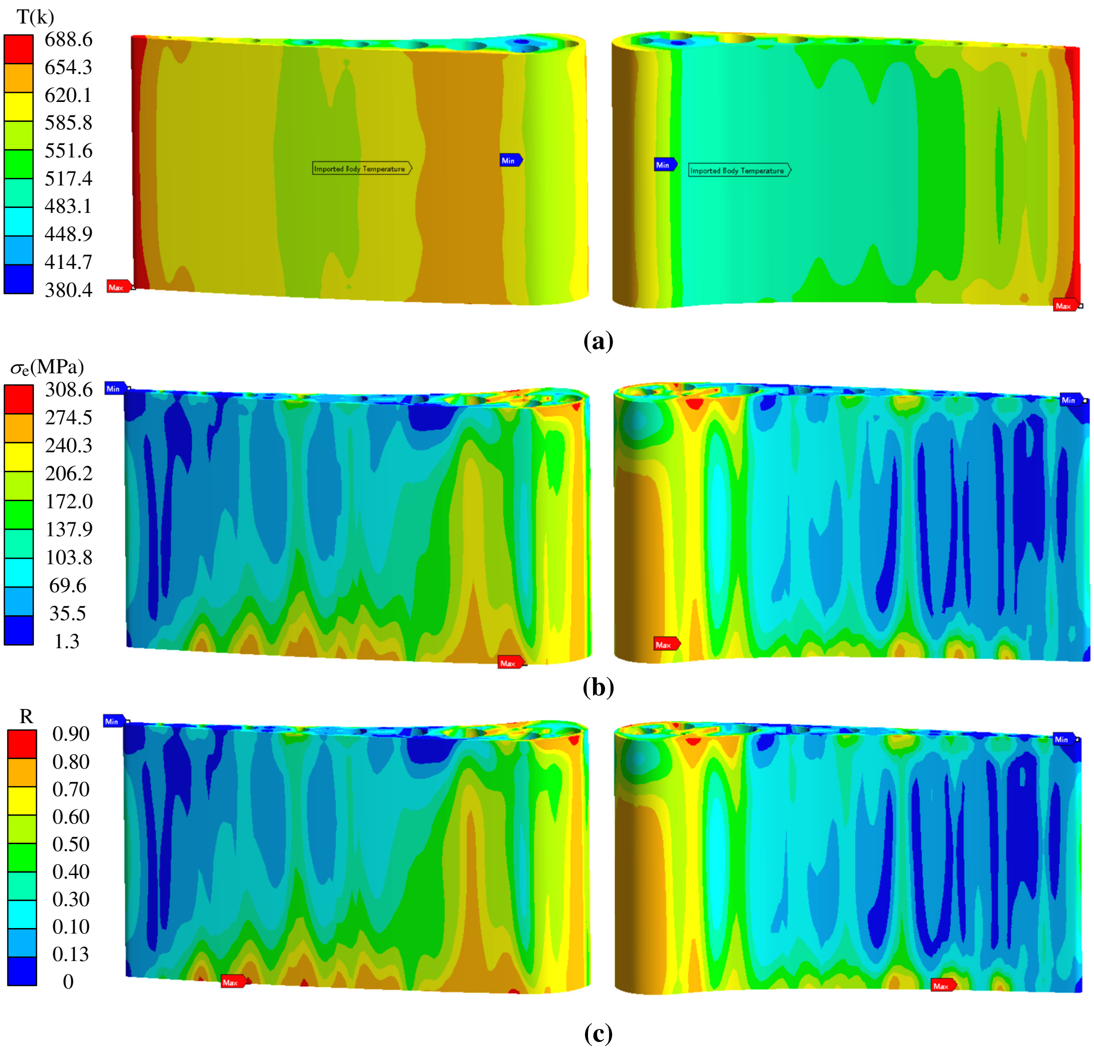

Figure 14: Simulation results for the Mark-II TGV at a maximum stress ratio of 0.9. (**a**) Temperature. (**b**) Equivalent stress. (**c**) Stress ratio.

4 Conclusions

In this study, a flow-thermo-structural model is established based on the geometric configuration of the Mark-II TGV. Subsequently, the mass and strength of the Mark-II TGV are comprehensively optimized using OED, RSM, and GA, focused on highly sensitive variables. The key conclusions are summarized as follows:

(1) The convective heat transfer coefficient of the cooling channels is employed instead of a detailed cooling air model. This approach not only circumvents mesh generation complexities but also reduces computational workload. The discrepancy between the simulation and experimental results is less than 7.5%, thereby validating the reliability of the flow-thermo-structural model.

(2) A stress ratio parameter is proposed for the strength analysis of the TGV to comprehensively account for plastic limits at varying temperatures. The application of OED reduces the ten factors in RSM to six highly sensitive variables, decreasing the number of calculations from 542 to 86 and significantly enhancing optimization efficiency.
(3) An optimization method incorporating constraints is established by combining OED, GA, and RSM. Under constraint conditions where the stress ratio does not exceed 0.95 and 0.9, the optimal masses are 0.857 and 0.881 kg, respectively. These represent total mass reductions of 16.80% and 14.47% compared to the standard model. The maximum stress ratios after optimization are 0.94 and 0.9, respectively, aligning closely with the constraints and confirming the reliability of the predicted optimal designs. Furthermore, the location of the maximum stress ratio differs from that of the maximum stress, demonstrating the necessity of introducing stress ratio analysis.

Acknowledgement: Not applicable.

Funding Statement: Supported by the Liaoning Provincial Department of Science and Technology Joint Program (General Program) (No. 2025-MSLH-556).

Author Contributions: Peng Guan: Conceptualization, Methodology, Software, Validation, Formal analysis, Writing—original draft, Investigation, Resources, Visualization. Ming-Ran Li: Conceptualization, Data curation, Formal analysis, Writing—review & editing, Supervision. Si-Bo-Wen Wang: Methodology, Software, Investigation. All authors reviewed and approved the final version of the manuscript.

Availability of Data and Materials: The authors confirm that the data supporting the findings of this study are available within the article and its supplementary materials.

Ethics Approval: Not applicable.

Conflicts of Interest: The authors declare no conflicts of interest.

References

1. Lakshminarayana B. Fluid dynamics and heat transfer of turbomachinery. New York, NY, USA: John Wiley & Sons; 1996. doi:10.1002/9780470172629.
2. Hu K, Wang X, Zhong S, Lu C, Yu B, Yang L, et al. Optimization of turbine blade trailing edge cooling using self-organized geometries and multi-objective approaches. Energy. 2024;289(2):130013. doi:10.1016/j.energy.2023.130013.
3. Hermansen SM, Lund E. Multi-material and thickness optimization of a wind turbine blade root section. Struct Multidiscip Optim. 2024;67(7):107. doi:10.1007/s00158-024-03811-0.
4. Balijepalli R, Chandramohan VP. Optimization of design parameters of wind turbine blade for a solar chimney plant using betz and Bernoulli's theories. Arab J Sci Eng. 2024;49(8):11367–80. doi:10.1007/s13369-023-08655-2.
5. Immarigeon JP, Holt RT, Koul AK, Zhao L, Wallace W, Beddoes JC. Lightweight materials for aircraft applications. Mater Charact. 1995;35(1):41–67. doi:10.1016/1044-5803(95)00066-6.
6. Deng X, Wang J, Zhou J, Shen H, Shen Z, Zhang J, et al. A hybrid cellular automaton method for structural topology optimization with mechanical and heat constraints. Front Heat Mass Transf. 2019;12(1):1–6. doi:10.5098/hmt.12.13.
7. Hamlaoui MN, Bouhelal A, Smaili A, Khelladi S, Fellouah H. An inverse CFD actuator disk method for aerodynamic design and performance optimization of Horizontal Axis Wind Turbine blades. Energy Convers Manag. 2024;316(2):118818. doi:10.1016/j.enconman.2024.118818.
8. Su Z, Zhang B, Zhu J, You Y. Novel design method for tilting electric-drive ducted fan blades with dual-operation conditions. Aerosp Sci Technol. 2026;173(2):111786. doi:10.1016/j.ast.2026.111786.
9. Mackolil J, Basavarajappa M, Lorenzini G. Thermodynamic analysis of Marangoni convection in magnetized nanofluid. Front Heat Mass Transf. 2025;23(2):529–51. doi:10.32604/fhmt.2025.058702.

10. Ayeb M, Turki M, Frija M, Fathallah R. Fatigue prediction and optimization of laser peened turbine blade using artificial neural networks and ANFIS. Fatigue Fract Eng Mat Struct. 2024;47(11):4030–47. doi:10.1111/ffe.14409.
11. Shi J, Zhou J, Lyu Y, Lu J. Parallel grid search-enhanced support vector regression for small unmanned helicopter modeling. Eng Comput. 2026;43(1):349–62. doi:10.1108/ec-02-2025-0104.
12. Zhang X, Wang Y, Lei Q, Zhao J, Ai Y. Surrogate model-based optimization of a dual-shield total temperature probe for aero-engine applications. Mathematics. 2025;13(23):3870. doi:10.3390/math13233870.
13. Yang W, Lin Y, Hu J, Li F, Wang F, Yao J. Reduced-order model of complex unsteady flows in turbomachinery based on direct proper orthogonal decomposition and optimized radial basis function. Int J Comput Methods. 2026;23(4):2550064. doi:10.1142/s0219876225500641.
14. Wei J, Zheng Q, Yan W, Jiang B. Probability analysis of compressor blade vibration based on radial basis function extremum neural network method. Proc Inst Mech Eng Part O J Risk Reliab. 2025;239(5):1070–85. doi:10.1177/1748006x241298540.
15. Afrin N, Lopez J, Ocampo J. Kriging surrogate based optimization of thermal damage to living biological tissues by laser irradiation based on a generalized dual phase lag model. Front Heat Mass Transf. 2022;18(1):1–7. doi:10.5098/hmt.18.46.
16. Zhang X, Lu Z, Cheng K. AK-DS: an adaptive Kriging-based directional sampling method for reliability analysis. Mech Syst Signal Process. 2021;156(15):107610. doi:10.1016/j.ymssp.2021.107610.
17. Guo C, Sun Y, Yu R, Peng C. Metamodeling of turbofan engine compressor characteristics using SVM-based improved Kriging method. Aircr Eng Aerosp Technol. 2025;97(2):212–22. doi:10.1108/aeat-03-2024-0064.
18. Li ZA, Dong XW, Zhu CY, Chen CH, Zhang H. Vectorial surrogate modeling method based on moving Kriging model for system reliability analysis. Comput Meth Appl Mech Eng. 2024;432(1):117409. doi:10.1016/j.cma.2024.117409.
19. Ma T, Xi X, Zhao C, Xu Y, Zhang H, Liu H. A locally enhanced physics-informed neural network surrogate model for rapid aerothermal assessment of aero-engine nozzles. Aerosp Sci Technol. 2026;168(10):111002. doi:10.1016/j.ast.2025.111002.
20. Yamashita D, Tanaka H, Ikami T, Nagai H. Transient system-wide surrogate model for spacecraft thermal analysis using recurrent neural networks with POD data reduction. Int J Heat Mass Transf. 2026;255(7):127854. doi:10.1016/j.ijheatmasstransfer.2025.127854.
21. Chen L, Qin T, Gao W, Zeng H, Han Z. Aerodynamic shape optimization of rockets based on a multi-fidelity neural network surrogate model. J Phys Conf Ser. 2025;3109(1):012066. doi:10.1088/1742-6596/3109/1/012066.
22. García Nieto P, García-Gonzalo E, Bernardo Sánchez A, Menéndez Fernández M. A new predictive model based on the ABC optimized multivariate adaptive regression splines approach for predicting the remaining useful life in aircraft engines. Energies. 2016;9(6):409. doi:10.3390/en9060409.
23. Tang X, Luo J, Liu F. Aerodynamic shape optimization of a transonic fan by an adjoint-response surface method. Aerosp Sci Technol. 2017;68(2):26–36. doi:10.1016/j.ast.2017.05.005.
24. Yu M, Shi C, Liu Z, Liu W. Design and multi-objective optimization of a new annular constructal bifurcation Stirling regenerator using response surface methodology. Int J Heat Mass Transf. 2022;195(1):123129. doi:10.1016/j.ijheatmasstransfer.2022.123129.
25. Gallis P, Salvadori S, Misul DA. Numerical analysis of a flow control system for high-pressure turbine vanes subject to highly oscillating inflow conditions. In: Proceedings of the ASME Turbo Expo 2024: Turbomachinery Technical Conference and Exposition; 2024 Jun 24–28; London, UK. p. V005T06A021. doi:10.1115/gt2024-126791.
26. Jiang Y, Tao Z, Li H, Zhou Z. Shape optimization of the laidback fan-shaped film cooling hole on pressure surface of turbine guide vane. In: Proceedings of the ASME Turbo Expo 2022: Turbomachinery Technical Conference and Exposition; 2022 Jun 13–17; Rotterdam, The Netherlands. p. V06AT12A025. doi:10.1115/gt2022-82358.
27. Huang Y, Zhang JZ, Wang CH, Zhu XD. Multi-objective optimization of laidback fan-shaped film cooling hole on Turbine Vane Suction Surface. Heat Mass Transf. 2019;55(4):1181–94. doi:10.1007/s00231-018-2500-6.
28. Zhang L, Cao G, Feng K, Jia Y, Zhang Z. Improvement of multi-hole airflow impingement on flow and heat transfer characteristics inside a turbine vane cavity. Appl Sci. 2021;11(21):9924. doi:10.3390/app11219924.

29. Wang B, Zhang W, Xie G, Xu Y, Xiao M. Multiconfiguration shape optimization of internal cooling systems of a turbine guide vane based on thermomechanical and conjugate heat transfer analysis. J Heat Transf. 2015;137(6):061004. doi:10.1115/1.4029852.
30. Yu R, Han H, Yang C, Luo W. Optimal design and decision making of an air cooling channel with hybrid ribs based on RSM and NSGA-II. J Therm Anal Calorim. 2022;147(10):5839–54. doi:10.1007/s10973-021-10807-1.
31. Wang W, Tao G, Ke D, Ruan Z, Liu J, Luo J, et al. Multi-objective optimization of transpiration cooling for high pressure turbine vane. Appl Therm Eng. 2024;246(22):122926. doi:10.1016/j.applthermaleng.2024.122926.
32. Sun Z, Kong C, Niu X, Song Y, Wang X. Optimization and reliability analysis of 2.5D C/SiC composites turbine stator vane. Appl Compos Mater. 2014;21(5):789–803. doi:10.1007/s10443-013-9374-z.
33. Chi Z, Ren J, Jiang H. Coupled aerothermodynamics optimization for the cooling system of a turbine vane. J Turbomach. 2014;136(5):051008. doi:10.1115/1.4025178.
34. van de Noort M, Ireland PT. Genetic algorithm-based optimisation of a double-wall effusion cooling system for a high-pressure turbine nozzle guide vane. Int J Turbomach Propuls Power. 2024;9(1):6. doi:10.3390/ijtpp9010006.
35. Andrew AM. Systems: an introductory analysis with applications to biology, control, and artificial intelligence, by John H. Holland MIT Press (Bradford Books), Cambridge, Mass., 1992, xiv+211 pp. (Paperback £13.50, cloth £26.95). Robotica. 1993;11(5):489. doi:10.1017/s0263574700017136.
36. Hylton LD, Mihelc MS, Turner ER, Nealy DA, York RE. Analytical and experimental evaluation of the heat transfer distribution over the surfaces of turbine vanes. Cleveland, OH, USA: NASA Lewis Research Center; 1983. Report No.: NASA CR-182133.
37. Editorial Committee of China Aviation Materials Manual. Handbook of aeronautical materials of China (Volume II): Wrought and cast superalloys. Beijing, China: China Standard Press; 2002.
38. Guan P. Study on nozzle guide vane subjected to high-temperature shock by thermal/flow/structure coupling method [dissertation]. Xi'an, China: Northwestern Polytechnical University; 2020. doi:10.27406/d.cnki.gxbgu.2020.000061.
39. Dong P. Research on conjugate heat transfer simulation of aero turbine engine air-cooled vane [dissertation]. Harbin, China: Harbin Institute of Technology; 2009.
40. Gnielinski V. New equations for heat and mass transfer in turbulent pipe and channel flows. Int Chem Eng. 1976;16:359–68.
41. Xiong Y, Pan Y, Wu L, Liu B. Effective weight-reduction- and crashworthiness-analysis of a vehicle's battery-pack system via orthogonal experimental design and response surface methodology. Eng Fail Anal. 2021;128(2017):105635. doi:10.1016/j.engfailanal.2021.105635.
42. Li JT, Liu ZJ, Jabbar MA, Gao XK. Design optimization for cogging torque minimization using response surface methodology. IEEE Trans Magn. 2004;40(2):1176–9. doi:10.1109/tmag.2004.824809.
43. Montgomery DC. Design and analysis of experiments. 9th ed. New York, NY, USA: John Wiley & Sons; 2017.
44. Sun Y, Cai L, Chen Y, Wang S. Optimization of a high through-flow design turbine using response surface method. Phys Fluids. 2024;36(4):046106. doi:10.1063/5.0202374.